SAR AND OPTICAL SENSOR DATA FUSION FOR EARTHQUAKE DAMAGE ASSESSMENT AND ANALYSIS OF THE SIGNIFICANT FEATURES

Gunjan Joshi[1], Ryo Natsuaki[2] and Akira Hirose[3]
[1,2,3] Department of Electrical Engineering and Information Systems, The University of Tokyo 7-3-1 Hongo, Bunkyo-ku, Tokyo 113-8656, Japan
[1]Email: gunjanjoshi88@g.ecc.u-tokyo.ac.jp
[2]Email: natsuaki@ee.t.u-tokyo.ac.jp
[3]Email: ahirose@ee.t.u-tokyo.ac.jp

KEY WORDS: Synthetic aperture radar, Optical satellite, Neural network, earthquake damage detection, Inverse-mapping

ABSTRACT: The resolution and detection capabilities of synthetic aperture radars (SAR) and optical sensors have increased significantly in the past decade to detect damages of earthquakes. However, the processing and analysis of large-area images obtained by these sensors is labor-intensive, time-consuming, and requires domain expertise. Recently, the use of neural networks has been a great asset in this regard. This paper proposes a neural network that combines relevant features from a SAR and an optical sensor. This multi-sensor-fusion neural network has been used for earthquake damage detection in Sulawesi, Indonesia. We also propose inverse-mapping dynamics that aims to understand the significant input features that are impactful for the output of the neural network.

1. INTRODUCTION

Damage mapping is essential in the prevention of life and property post a disaster. Large-scale disasters such as earthquakes and landslides damage the transportation routes making the calamity stricken area inaccessible via ground. SAR satellites and optical satellites play a vital role in this scenario by providing a large amount of valuable information about the area of interest (AOI). SAR sensors that are highly sensitive to changes on the earth's surface can image at any time of the day and in any weather conditions (Stramondo et al. 2006). Whereas, optical sensors can provide us with easy-to-understand surface information. Conventional methods of disaster damage mapping using these sensors involved comparing the respective image from before and after the disaster (Natsuaki et al. 2018; Syifa, Kadavi, and Lee 2019; Tamkuan and Nagai 2017). Previous studies (De Alban et al. 2018) on the fusion of both sensors have shown that integrating data from both sensors can increase the detection sensitivity and provide more accurate information about the area under observation. Analyzing the large amount of information provided by the sensors is labor-intensive. Thus, we propose the use of a neural network that combines features from both SAR and optical sensors. Since we use features from two sensors in this study, it is necessary to evaluate what features from which sensor are prominent, which we accomplish by using inverse-mapping dynamics.

2. SAR AND OPTICAL DATA FUSION BY USING A FULLY CONNECTED NEURAL NETWORK

2.1 Study area

An earthquake of magnitude 7.5 struck the coast of Sulawesi in Indonesia on September 28, 2018. Among other damages, this earthquake was responsible for generating multiple landslides and a tsunami. The epicenter was the Donggala Regency, 80km north of the city of Palu. The greatest loss of life in this disaster can be attributed to the landslides that led to voluminous debris flow (Bradley et al. 2019). In this paper, we generate the post-disaster map of the Sidera region shown in Figure 1, where large-scale soil liquefication led to high fatalities (Goda et al. 2019).

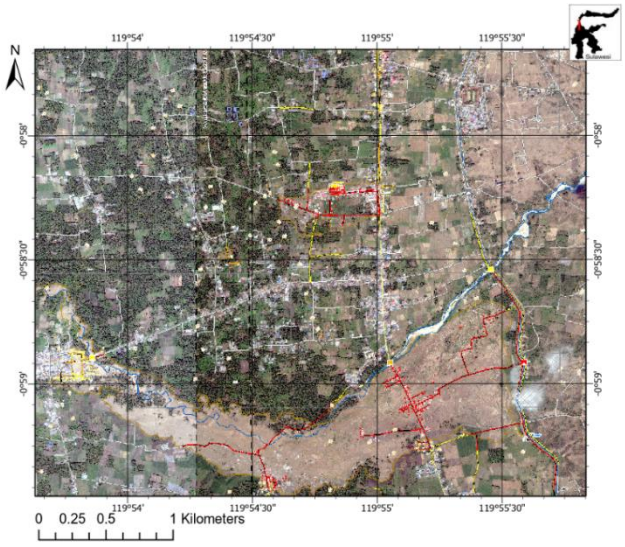

Figure 1: Map of Sidera region in Sulawesi, Indonesia, depicting the landslide (Copernicus Emergency Management Service).

2.2 Dataset

The damages were mapped using the L-band SAR sensor Advanced Land Observation Satellite-2 (ALOS-2) of the Japan Aerospace Exploration Agency (JAXA) and the optical Sentinel-2 sensor of the European Space Agency (ESA). The various datasets used are described in Table 1.

Table 1: Datasets used in this study.

Satellite	Type	Date	
ALOS - 2	**SAR**	**11 May 2018**	**Pre-Event**
ALOS - 2	**SAR**	**17 Aug 2018**	**Pre-Event**
Sentinel - 2	**Optical**	**02 October 2018**	**Pre-Event**
Sentinel - 2	**Optical**	**27 September 2018**	**Post-Event**
ALOS - 2	**SAR**	**12 October 2018**	**Post-Event**

2.3 Feature Extraction

We extracted features that are considered informative for damage detection from SAR and optical data. The pre-processing steps have been illustrated in Figure 2. The SAR data were obtained in Horizontal-Horizontal (HH) and Horizontal-Vertical (HV) polarizations. Thus from the SAR data, intensity and coherence were extracted in both polarization, whereas from the optical sensor Normalised Difference Vegetation Index (NDVI), Normalized Difference Building Index (NDBI), and the Build-Up index (BUI) were extracted. All the features were extracted both before and after the disaster.

- Intensity is the backscattering received by the SAR sensor. Comparing the intensity before and after the disaster can provide us with useful information about the disaster (Ge et al. 2019), given as

$$\text{Intensity} = (\text{Amplitude})^2 \tag{1}$$

- Coherence is a parameter that depicts the stability of a region, subtle changes in the surface can be detected with high levels of accuracy using this feature (Havivi et al. 2018). It is given as

$$\text{Coherence} = \frac{|\langle (\boldsymbol{S})^* \boldsymbol{P} \rangle|}{\sqrt{\langle (\boldsymbol{P})^* \boldsymbol{P} \rangle \langle (\boldsymbol{S})^* \boldsymbol{S} \rangle}} \tag{2}$$

Where $\boldsymbol{P}$ and $\boldsymbol{S}$ represent horizontally or vertically received electric fields in vectors obtained by primary

and secondary observations, and $(\cdot)^*$ above them represents the complex conjugate, and the bracket denotes the spatial average for 3×3 window.

- NDVI is an index obtained from optical data and classifies the area based on the vegetation. It is given by the contribution of the satellite bands corresponding to the Red wavelength and Near-Infrared (NIR) wavelength. Red and NIR bands correspond to Band-4 and Band-8 of Sentinel-2, respectively (Kuc and Chormański 2019).

$$\mathrm{NDVI} = \frac{\mathrm{NIR} - \mathrm{Red}}{\mathrm{NIR} + \mathrm{Red}} \tag{3}$$

- NDBI is an index that highlights the urban areas in the optical data and is given by the normalization of the Short-Wave-Infra-Red (SWIR) and Near Infra-Red (NIR) wavelengths, Band-11 of Sentinel -2 corresponds to the SWIR wavelength (Osgouei et al. 2019), NDBI is calculated as

$$\mathrm{NDVI} = \frac{\mathrm{SWIR} - \mathrm{NIR}}{\mathrm{SWIR} + \mathrm{NIR}} \tag{4}$$

- BUI is the index for the analysis of urban patterns using NDVI and NDBI. A higher value of a pixel in this index indicates a higher possibility that it represents a built-up area (Bhatti and Tripathi 2014), which allows built-up areas to be mapped effectively. BUI is given as

$$\mathrm{BUI} = \mathrm{NDBI} - \mathrm{NDVI} \tag{5}$$

To ensure geometric accuracy, the seven pre-seismic features and the seven post-seismic features were collocated so that all the corresponding pixels in the fourteen features are mapped to the same geographical location. Following this, the datasets were clipped to the coordinates of the AOI and normalized between -1 and $+1$.

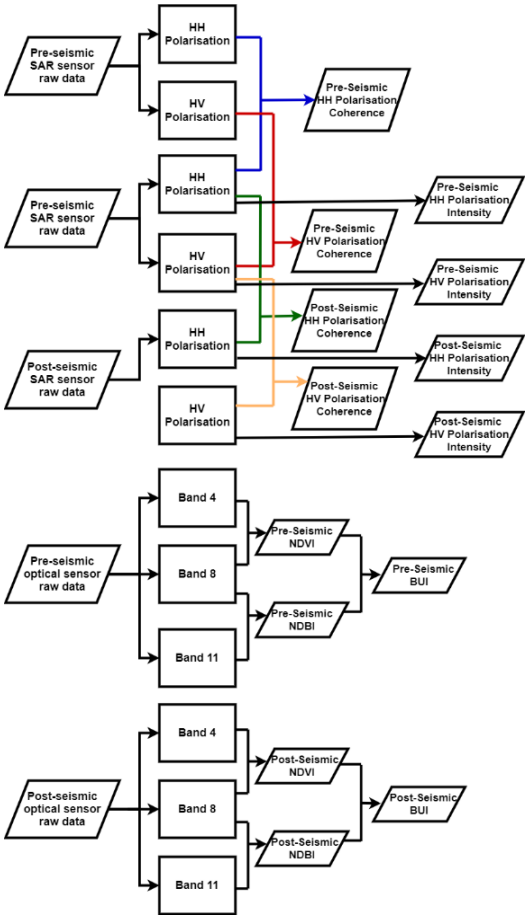

Figure 2: Pre-processing for SAR and optical raw data.

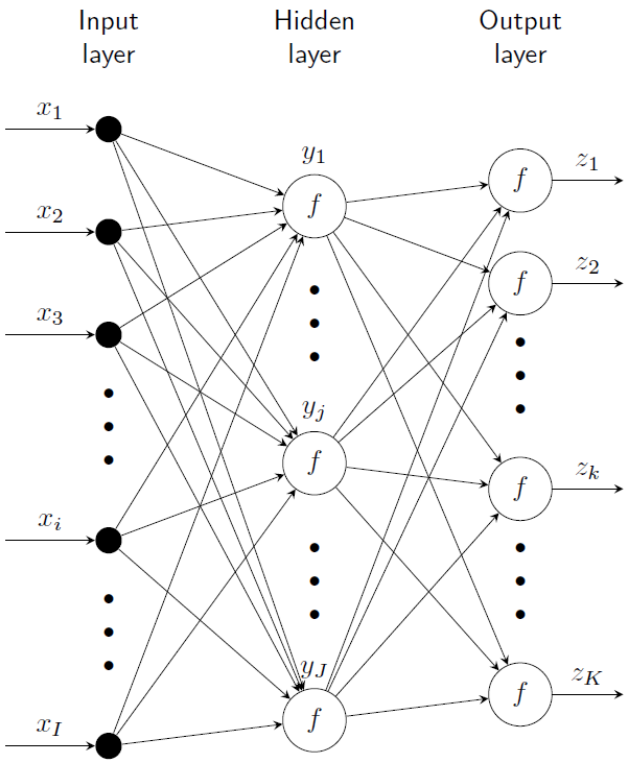

Figure 3: Forward processing neural network.

2.4 Neural network classification

Neural network modeling is a reliable tool for data classification that is applicable across several fields as these networks can analyze and learn complex data. In this work, we propose a neural network that estimates the land classification and predicts if the land type is damaged or not.

As shown in Figure 3, the neural network is a multi-layer network with a 14-neuron input layer, 64-neuron hidden layer, and a 7-neuron output layer. The input layer is fed with pixel-by-pixel values of the fourteen feature images obtained after the pre-processing. At the output layer, the neural network classifies each pixel as one of the seven land type classes, namely, damaged forest, damaged irrigation field, damaged urban, undamaged forest, undamaged irrigation, undamaged urban, and undamaged dryland regions.

Considering $\boldsymbol{x} = [x_1\ x_2\ \dots\ x_i\ \dots\ x_I]^{\mathrm{T}}$, $\boldsymbol{y} = [y_1\ y_2\ \dots\ y_j\ \dots\ y_J]^{\mathrm{T}}$ and $\boldsymbol{z} = [z_1\ z_2\ \dots\ z_k\ \dots\ z_K]^{\mathrm{T}}$ (T = transpose) to be input, hidden, and output signal respectively, and $\mathbf{W_1}$ and $\mathbf{W_2}$ to be the weights obtained after the learning phase, the values at the last layer of the neural network can be evaluated as

$$\begin{aligned} \boldsymbol{z} &= f(\mathbf{W_2}\boldsymbol{y}) \\ &= f\big(\mathbf{W_2}\, f(\mathbf{W_1}\boldsymbol{x})\big) \end{aligned} \tag{6}$$

where f represents the activation function working component-wise and defined by

$$f(x) = \begin{cases} -\log(-x-1)) & \text{if } x < 0 \\ 0 & \text{if } x = 0 \\ \log\,(x+1) & \text{if } x > 0 \end{cases} \tag{7}$$

The rationale for not using the conventionally used activation functions such as tanh or ReLU is that the use of these activation functions led to a limited range of inversely input values in the inverse mapping, which can be avoided by using the modified logarithmic function defined in (7). The neural network was trained on 3970 pixels of the Sidera AOI, shown enclosed in the black boxes in Figure 4, 794 pixels of which are used to validate the network. The network was trained for 1000 epochs. The ground-truth classes were derived from the land classification published in Bradley et al. 2019 and modified for damaged areas based on data from Copernicus Emergency Management Service.

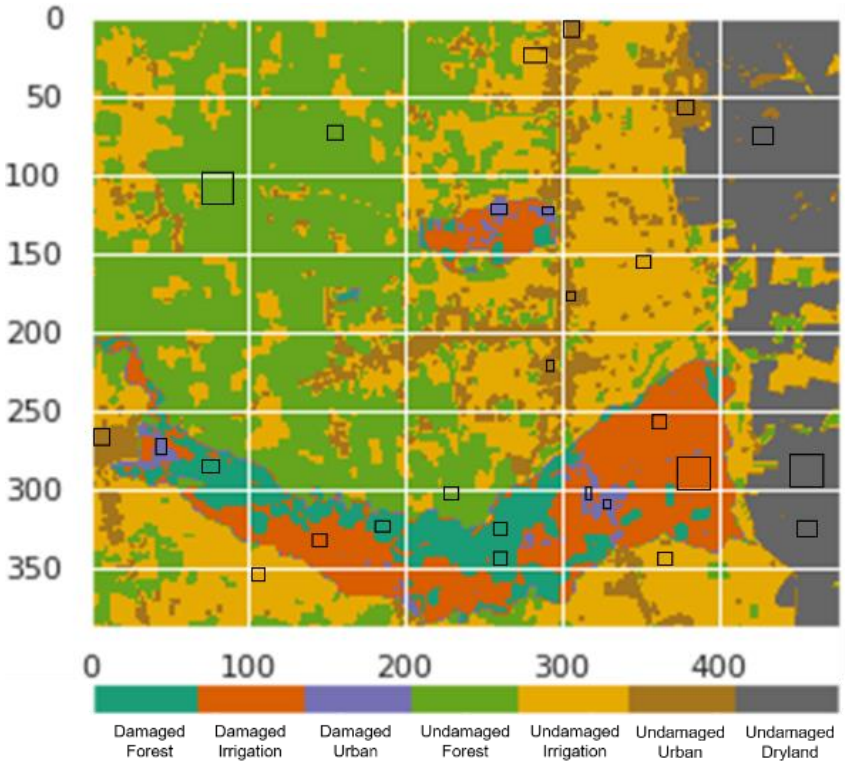

Figure 4: Land classification ground truth of the Sidera AOI (modified from Bradley et al. 2019).

Post-training, the neural network was applied on all the pixels of the AOI, and each pixel was classified as one of the seven landtypes.

2.5 Inverse-mapping dynamics

Inverse mapping is dynamics that traces which input is significant for which output by paying attention to the signal flow of the network. In this process, the values obtained at the winning node $\hat{k}$, of the forward neural network was fed to the same node at the input of the inverse mapping, as shown in Figure 5, while all the other nodes were fed with zeros. This was done to suppress any influence that could be introduced by the non-significant classes. The output values can be obtained as

$$\tilde{\boldsymbol{x}} = \mathbf{W}_1^{\mathrm{T}} f^{-1}(\mathbf{W}_2^{\mathrm{T}} f^{-1}(\tilde{\boldsymbol{z}})) \tag{8}$$

Where $\tilde{\boldsymbol{z}} = [0\ 0\ \ldots\ z_{\hat{k}}\ \ldots\ 0]^{\mathrm{T}}$ is the modified output values of the forward processing network fed as an input to the inverse-mapping network, $\tilde{\boldsymbol{x}}$ is the output of the inverse-mapping network, and the inverse activation function f^{-1} is defined as

$$f^{-1}(x) = \begin{cases} -\mathrm{e}^{-x} + 1 & \text{if } x < 0 \\ 0 & \text{if } x = 0 \\ \mathrm{e}^{x} - 1 & \text{if } x > 0 \end{cases} \tag{9}$$

Inverse-mapping is performed for all the pixels, and the features that showed high significance are determined by the use of box and whisker plots.

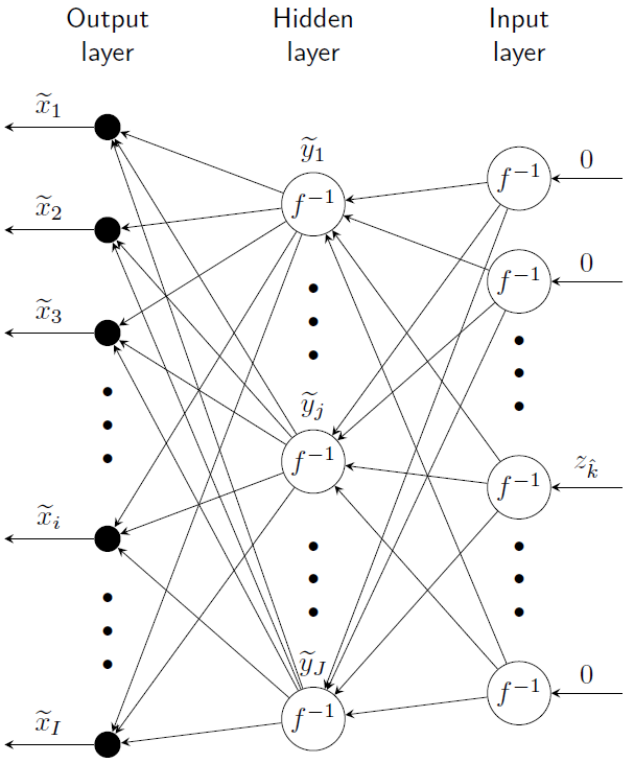

Figure 5: Inverse-mapping network.

3. RESULTS

3.1 Pre-processing results

Table 2 illustrates the features extracted from the multiple sensors. After the disaster, an increase in the brightness can be observed in areas affected by the calamity for the SAR intensity feature in both HH and HV polarization. Additionally, loss in coherence can be observed for the same region in both polarizations. In the case of the optical parameters as well, changes can be observed in the features post the disaster. NDVI tends to decrease in regions that had a loss of vegetation following the disaster. Furthermore, the NDBI and BUI increased in landslide-affected areas as the vegetated land got converted to barren land.

Table 2: The images obtained after pre-processing, that are used as input to the neural network.

Features	Pre-event image	Post-event image
RGB reference image	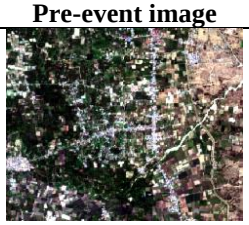	
Intensity HH	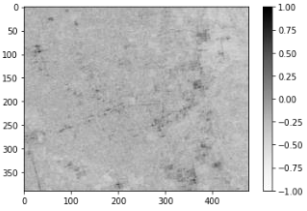	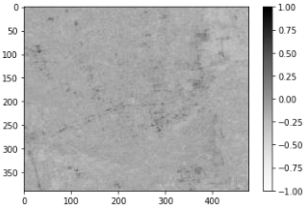
Intensity HV	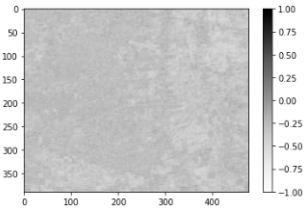	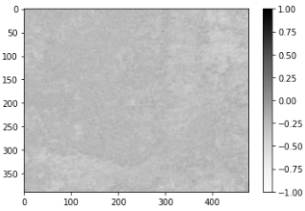
Coherence HH	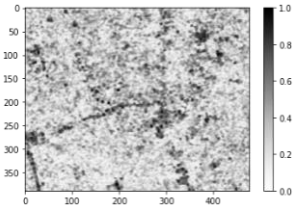	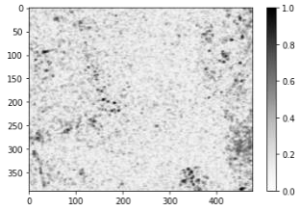
Coherence HV	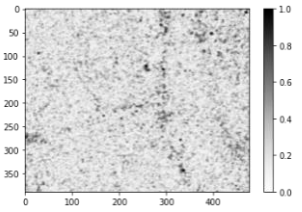	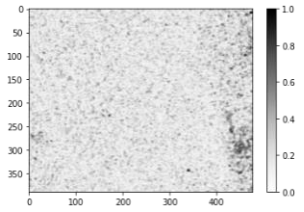
NDVI	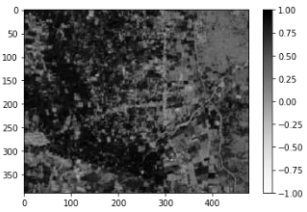	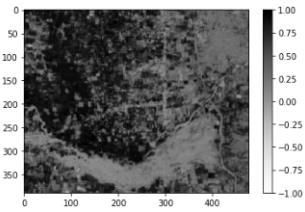
NDBI	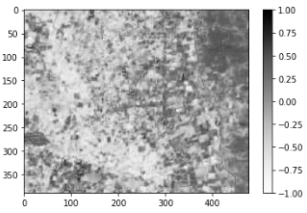	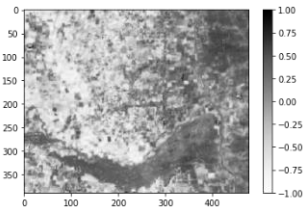
BUI	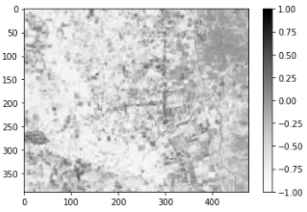	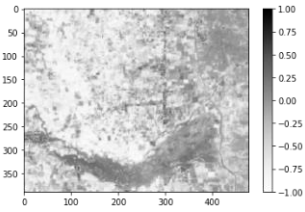

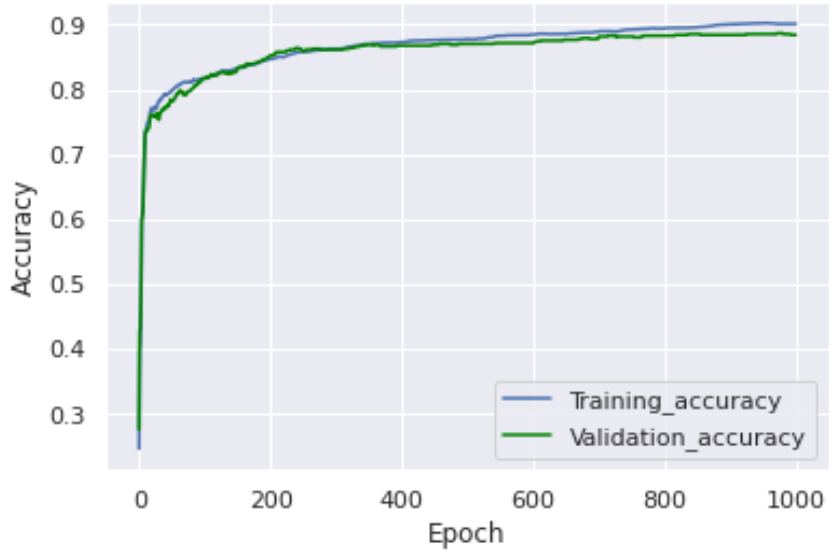

Figure 6: Training and validation accuracy of neural network.

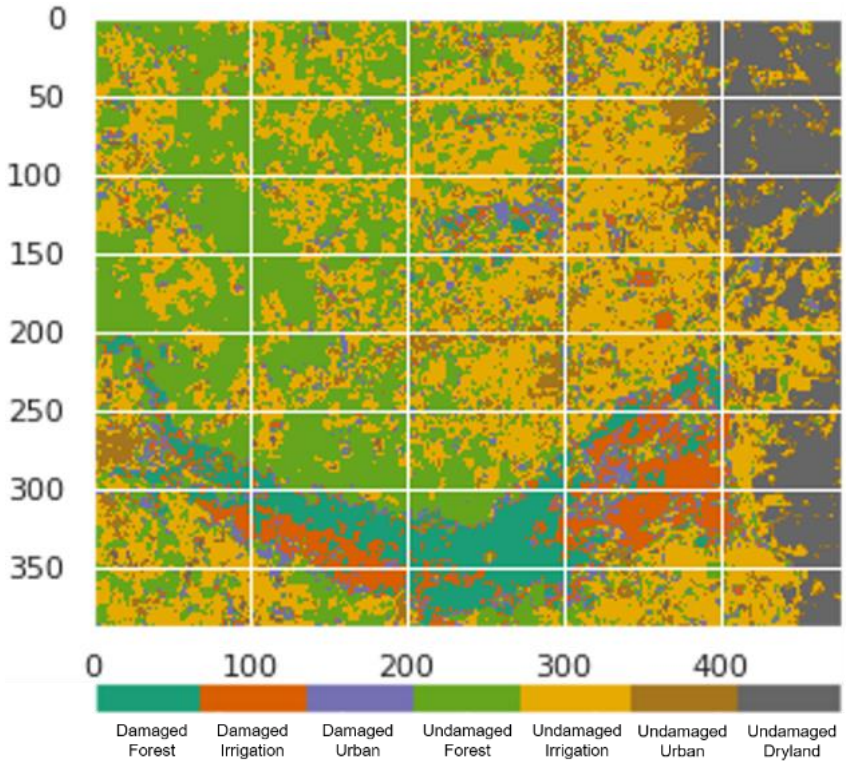

Figure 7: Neural network land classification result.

3.2 Classification results

Figure 6 shows the training and validation accuracy of the neural network. The network obtained 90.11% and 88.04% training and validation accuracy, respectively. Figure 7 illustrates the result of the neural network. Comparing this result with the ground truth in Figure 4, it can be observed that two landslide regions in this AOI were well detected by the neural network, and overall the neural network is able to classify the regions accurately.

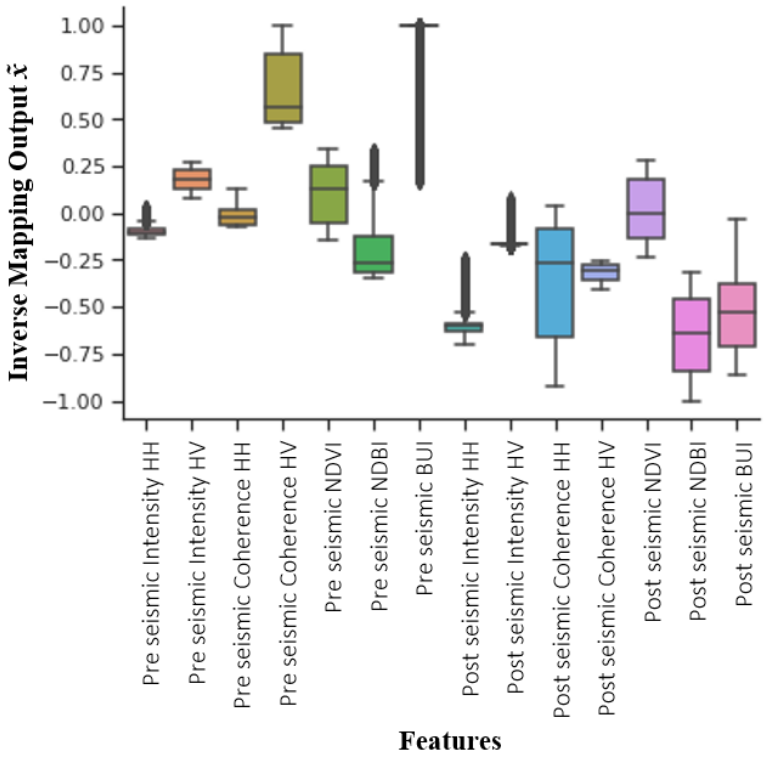

Figure 8: Inverse-mapping results for the damaged urban class.

3.3 Inverse-mapping results

Box and whisker plots were generated for each pixel. The significance of the features is illustrated by the density of the pixels near -1 or $+1$. Figure 8 shows the inverse-mapping output for the pixels classified as damaged urban. It can be observed that the pre-seismic BUI, pre-seismic coherence in HV polarization, and post-seismic NDBI show prominence in the detection of this class since they distribute near -1 or $+1$.

4. Discussion

Classification map was generated using features extracted from both ALOS-2 and Sentinel-2 data. The classification divided the land into seven classes. Through a visual inspection of the ground truth and the classification map, it can be seen that damaged areas were detected quite well, particularly in the detection of the landslide shape. NDBI, BUI, and coherence are independently considered to be good indicators of detecting changes in urban areas (Bhatti and Tripathi 2014; Natsuaki et al. 2018; Zha, Gao, and Ni 2003). In this study, it can be observed that these parameters worked collaboratively in urban damage detection. This method was applied to various AOI, and consistency in the results was observed. Traditionally, pre-seismic and post-seismic images of one feature are used for damage assessment. A noteworthy observation here is that complementary features do not work together when used with other features. Investigation of this observation can be the future scope of this work.

5. Conclusion

In this paper, we proposed the neural network that combines the capabilities of various damage indicating features obtained from SAR and optical sensors to estimate the damages of the Sidera region. The combination of two sensors was found to be effective for land type detection and gave us consistent and reasonable results. Moreover, through this study, we were able to identify the relevance of these features to damage assessment. It was observed that features that independently contribute to damage detection of a particular class collaboratively determined that specific class. The features deemed as significant belong to both SAR and optical sensors, highlighting the necessity of sensor integration. This study illustrated that the synergetic use of multiple sensors could provide us with significant information that can help us understand the landscape dynamics better.

References from Journals:

Bhatti, Saad Saleem, and Nitin Kumar Tripathi. 2014. "Built-up Area Extraction Using Landsat 8 OLI Imagery." *GIScience and Remote Sensing* 51(4): 445–67.

Bradley, Kyle et al. 2019. "Earthquake-Triggered 2018 Palu Valley Landslides Enabled by Wet Rice Cultivation." *Nature Geoscience* 12(11): 935–39. http://dx.doi.org/10.1038/s41561-019-0444-1.

De Alban, Jose Don T., Grant M. Connette, Patrick Oswald, and Edward L. Webb. 2018. "Combined Landsat and L-Band SAR Data Improves Land Cover Classification and Change Detection in Dynamic Tropical Landscapes." *Remote Sensing* 10(2).

Ge, Pinglan, Hideomi Gokon, Kimiro Meguro, and Shunichi Koshimura. 2019. "Study on the Intensity and Coherence Information of High-Resolution ALOS-2 SAR Images for Rapid Massive Landslide Mapping at a Pixel Level." *Remote Sensing* 11(23).

Goda, Katsuichiro et al. 2019. "Cascading Geological Hazards and Risks of the 2018 Sulawesi Indonesia Earthquake and Sensitivity Analysis of Tsunami Inundation Simulations." *Frontiers in Earth Science* 7(February 2020).

Havivi, Shiran et al. 2018. "Combining TerraSAR-X and Landsat Images for Emergency Response in Urban Environments." *Remote Sensing* 10(5).

Kuc, G., and J. Chormański. 2019. "Sentinel-2 Imagery for Mapping and Monitoring Imperviousness in Urban Areas." *International Archives of the Photogrammetry, Remote Sensing and Spatial Information Sciences - ISPRS Archives* 42(1/W2): 43–47.

Natsuaki, Ryo, Hiroto Nagai, Naoya Tomii, and Takeo Tadono. 2018. "Sensitivity and Limitation in Damage Detection for Individual Buildings Using InSAR Coherence-A Case Study in 2016 Kumamoto Earthquakes." *Remote Sensing* 10(2).

Osgouei, Paria Ettehadi, Sinasi Kaya, Elif Sertel, and Ugur Alganci. 2019. "Separating Built-up Areas from Bare Land in Mediterranean Cities Using Sentinel-2A Imagery." *Remote Sensing* 11(3): 1–24.

Stramondo, S. et al. 2006. "Satellite Radar and Optical Remote Sensing for Earthquake Damage Detection: Results from Different Case Studies." *International Journal of Remote Sensing* 27(20): 4433–47.

Syifa, Mutiara, Prima Riza Kadavi, and Chang Wook Lee. 2019. "An Artificial Intelligence Application for Post-Earthquake Damage Mapping in Palu, Central Sulawesi, Indonesia." *Sensors (Switzerland)* 19(3).

Tamkuan, Nopphawan, and Masahiko Nagai. 2017. "Fusion of Multi-Temporal Interferometric Coherence and Optical Image Data for the 2016 Kumamoto Earthquake Damage Assessment." *ISPRS International Journal of Geo-Information* 6(7): 1–17.

Zha, Y., J. Gao, and S. Ni. 2003. "Use of Normalized Difference Built-up Index in Automatically Mapping Urban Areas from TM Imagery." *International Journal of Remote Sensing* 24(3): 583–94.

References from website:

Copernicus Emergency Management Service Retrieved June 16 2021 from https://emergency.copernicus.eu/mapping/list-of-components/EMSR317